

Giant power output in lead-free ferroelectrics by shock-induced phase transition

Zhipeng Gao,^{1,*} Wei Peng,² Bin Chen,³ Simon A. T. Redfern,^{3,4} Ke Wang,⁵ Baojin Chu,⁶ Qiang He,¹ Yi Sun,¹ Xuefeng Chen,² Hengchang Nie,² Wen Deng,³ Lingkong Zhang,³ Hongliang He,¹ Genshui Wang,^{2,7,†} and Xianlin Dong^{2,7}

¹National Key Laboratory of Shock Wave and Detonation Physics, Institute of Fluid Physics, China Academy of Engineering Physics, Mianyang 621900, China

²CAS Key Laboratory of Inorganic Functional Materials and Devices, Shanghai Institute of Ceramics, Chinese Academy of Sciences, Shanghai 200050, China

³Center for High Pressure Science and Technology Advanced Research, Shanghai 201203, China

⁴Department of Earth Sciences, University of Cambridge, Cambridge CB2 3EQ, United Kingdom

⁵State Key Laboratory of New Ceramics and Fine Processing, School of Materials Science and Engineering, Tsinghua University, Beijing 100084, China

⁶Information and Quantum Physics, University of Science and Technology of China, Hefei 230026, China

⁷The State Key Lab of High Performance and Superfine Microstructure Shanghai Institute of Ceramics, Chinese Academy of Sciences, Shanghai 200050, China



(Received 23 October 2018; published 11 March 2019)

The force-electric effect in ferroelectrics is characterized by the release of bound charge during pressure/shock-induced depolarization. In contrast to other electrical energy storage systems, the charge-storage/release by the force-electric effect of ferroelectrics is determined by polarization switching or polar-nonpolar phase transition. This offers a further set of options for materials design in the realm of energy conversion, especially for the high power density applications. Here, we report that a ferroelectric ceramic, $\text{Na}_{0.5}\text{Bi}_{0.5}\text{TiO}_3$ (NBT), can generate a high power output (3.04×10^8 W/kg) under shock compression, which is one of the highest values achieved by the force-electric effect. The *in situ* synchrotron x-ray diffraction studies reveal that this power output mainly arises from a polar-nonpolar phase transition (rhombohedral-orthorhombic). First-principles calculations show that this is a first-order phase transition that undergoes two-step structure changes. These results extend the application of the force-electric effect and are a key step in understanding the phase transition behaviors of NBT under high pressure.

DOI: [10.1103/PhysRevMaterials.3.035401](https://doi.org/10.1103/PhysRevMaterials.3.035401)

I. INTRODUCTION

Ferroelectric materials are characterized by their switchable spontaneous polarizations, which could be orientated by an applied electric field. After the poling process, ferroelectric materials retain bound charge associated with remnant polarizations (P_r). The poled ferroelectric materials show piezoelectric properties when they are operated at low strain and no large-scale disorientation of the ferroelectric domains occurs. When the applied stress/strain is high enough to reorientate the polarizations, the depolarization of the ferroelectrics would happen and the release of bound charge during depolarization can generate an electrical current. This process results in a loss of the P_r and a decrease or elimination of the piezoelectric effect. Sudden release of this charge by rapid depolarization through compression (high strain-rate loading) has been proposed as a source of rapid energy transfer [1–6]. This depolarization behavior is known as the force-electrical effect, or ferroelectric generator. Different from the batteries and electrochemical capacitors [6–9], the energy stored in these ferroelectric materials is stable while the charge-release

process is ultrafast, due to the charge-storage/release by this force-electric effect that is determined by P_r changing and polarization switching [9,10]. This behavior is important for applications that require portability, compactness, and high power density [11].

To maximize the power output density based on the force-electric effect, it is necessary to maximize P_r , increase the electrical breakdown field (E_b), and minimize the density of the ferroic solid [11–14]. The P_r determines the charge stored/released on the materials; the E_b is critical for increasing output voltage, while the density of the materials represents the mass [13,14].

The force-electric effect in ferroelectrics was firstly reported for barium titanate (BaTiO_3) in the 1950s [1]. Since the 1960s, lead zirconate titanate (PZT)-based compounds [9,10,15–19] largely replaced barium titanate and dominated this field for more than a half century. In the recent years, Shkuratov *et al.* carefully explored the force-electric properties of some ferroelectric single crystals and high- P_r ceramics [3,13,14,18–21]. They made great contributions to design materials and develop the high power applications. However, up to now, most studies of the force-electric effect have focused on its expression in the family of lead-based ferroelectric ceramics [14–21]. As the lead-free ferroelectric material investigated, BaTiO_3 shows a

*z.p.gao@foxmail.com

†genshuiwang@mail.sic.ac.cn

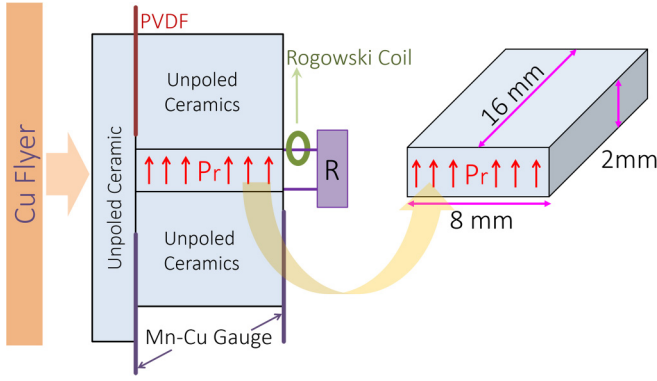


FIG. 1. Schematic of the dynamic compression experiments.

relatively poor force-electric effect due to its low P_r and low E_b [1].

Here, $\text{Na}_{0.5}\text{Bi}_{0.5}\text{TiO}_3$ (NBT) is explored as an alternative lead-free candidate for high power source, in view of its high P_r , high E_b , low density, and relatively high Curie temperature (T_c) [22,23]. The results show that the NBT could be fully depolarized by compression and generate a giant power output (3.04×10^8 W/kg). This power output is mainly attributed to a two-step polar-nonpolar phase transition from rhombohedral to orthorhombic under high pressure.

II. EXPERIMENTAL DETAILS

A. Materials preparations

The NBT ceramic samples were prepared by a conventional ceramic oxide synthesis. The crystal structure of the ceramics was characterized by x-ray diffraction (D/MAX-2550V; Rigaku, Tokyo, Japan), operated with Cu K α radiation at room temperature to confirm the single-phase nature of the material. The ceramic was cut with the dimension of $8 \times 2 \times 16$ mm. All the samples were poled under the same conditions of 9 kV/mm for 20 min. The thermal depoling experiment from room temperature to 400 °C was used to estimate the P_r value, which is $38 \pm 2 \mu\text{C}/\text{cm}^2$ (Supplemental Material, Fig. S1 [24]). This value is in the same range as the values reported for the NBT and its solid solutions, from 30 to $43 \mu\text{C}/\text{cm}^2$ [25–28]. The piezoelectric constant, d_{33} , of poled ceramics was measured as $\sim 78 \pm 3$ pC/N.

B. Dynamic compression experiments

The dynamic experiments setups are shown in Fig. 1. Plate impact experiments were applied to generate the shock wave, which offer several advantages for the investigation of dynamic behaviors over other techniques, including the ability to maintain the pressure during compression, good control of the duration time of shock wave, and to avoid the rarefaction wave [29–31]. In the experiments, a copper flyer was used as an impactor, which was fired by a gun and accelerated in the vacuum gun pipe. The Cu flyer impacted the sample at the end of the gun pipe and generated the shock wave to compress the samples. The schematic diagram for the dynamic experiments in the gun is shown in Fig. S2 (Supplemental Material). The compression direction is perpendicular to the P_r direction

of the ferroelectric ceramics in this study. The ferroelectric ceramics were packaged in the epoxy, for fixation and electrical insulation. As shown in Fig. 1, the ferroelectric polymer gauge, of polyvinylidene fluoride, was set on the front face and pressed against another unpoled sample to measure the shock pressure. Two Mn-Cu gauges were placed on the front and back surfaces of the poled ceramic to measure the travel time (τ) of the shock wave in the sample (Fig. S3). Five unpoled samples were placed on each side of the experimental sample to remove the effects of rarefaction waves, which would decrease the pressure during the experiments. In the external circuit, a Rogowski coil was used to measure the current and voltage across the resistance. All the signals were measured using an oscilloscope (TBS1000, Tektronix Inc., Cleveland, Ohio, USA).

In the high-power experiment, a poled NBT ceramic was connected in series with a 650- Ω resistor to generate high voltage. A compression pressure of 4.9 GPa was applied on the NBT ceramics. In the dynamic experiments with different compression pressures, the connected resistance is 1.0 Ω . The compression pressures were adjusted by the velocities of the copper flyer. In the study, the flyers speeds are 286, 408, 505, 617, 703, and 760 m/s, respectively. The wave velocity (u_s), particle velocity (u_p), and the densities (ρ_x) are calculated according to [32,33]

$$u_s = l/\tau, \quad (1)$$

$$\rho_x(u_s - u_p) = \rho_o(u_s - u_{p0}) \quad \text{Mass conservation equation,} \quad (2)$$

$$p - p_o = \rho_o(u_s - u_{p0})(u_p - u_{p0}) \quad \times \text{Momentum conservation equation,} \quad (3)$$

Where in this study l is 8.0 mm, which is the propagation length of the shock wave, τ is the duration of the shock wave in the ceramics, and u_s is the speed of the shock wave. The densities of the material before and after shock compression are ρ_o (5.85 g/cm³) and ρ_x , respectively. P_0 (0 GPa) and P are the pressures before and during the compression. Here, u_{p0} and u_p are the particle speeds before and during the shock compression, respectively, with $u_{p0} = 0$. Based on the three equations, l , τ , ρ_o , P_0 , P , and u_{p0} have been determined, so that u_p , u_s , and ρ_x can be obtained for experiments under different pressures. All the parameters are shown in Supplemental Material, Table S1 [24].

C. Static-compression experiment

High-pressure angle-dispersive x-ray diffraction (XRD) experiments were conducted using a symmetrical diamond-anvil cell at Beamline 12.2.2 of the Advanced Light Source, Lawrence Berkeley National Laboratory (Fig. S4). The XRD signal was collected with a MAR345 image plate. A T301 stainless-steel gasket with an initial thickness of about 40 μm and a hole of 150 μm in diameter was used to contain the sample. Finely ground NBT powders, alongside two ruby chips, were loaded within the pressure medium (a 4:1 methanol-ethanol mixture) into the hole in the gasket. The incident monochromatic synchrotron radiation beam had a wavelength 0.4959 \AA , and a beam size collimated to $\sim 25 \times 20 \mu\text{m}^2$. The diffraction pattern of CeO₂ was used to calibrate the

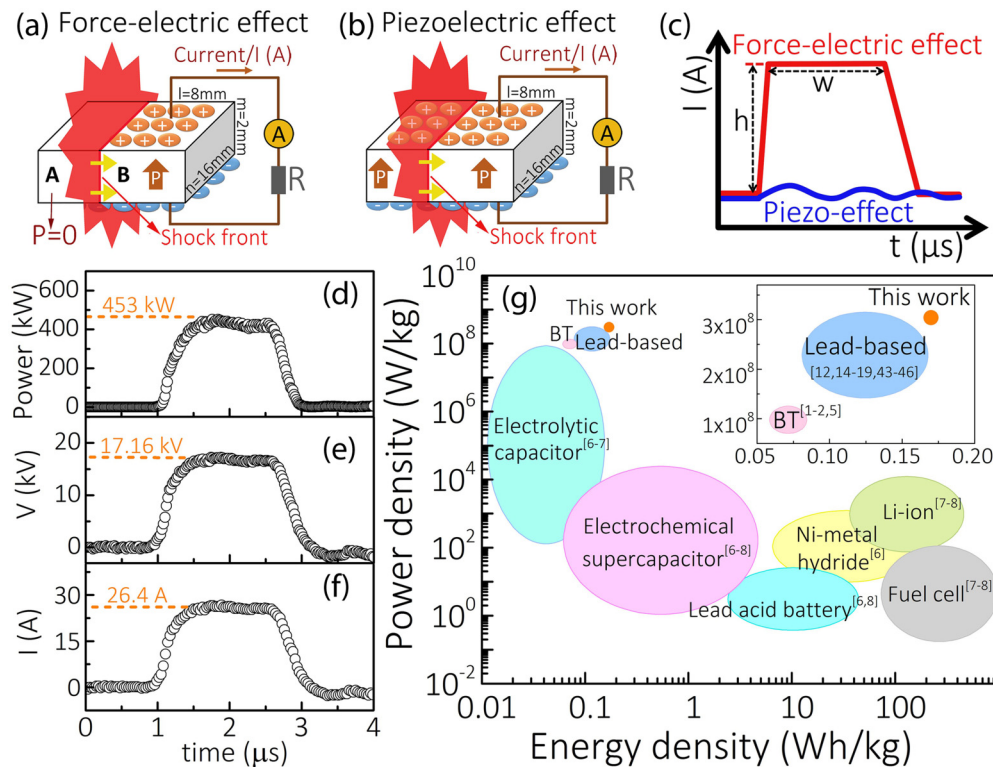


FIG. 2. Force-electric effect (a): The shock compression induces the depolarization with all bound charge released. Piezoelectric effect (b): The shock compression does not change the P_r value and the current in the external circuit is generated by the piezoelectric effect. The typical current wave forms generated by force-electric effect (red) and piezoelectric effect (blue) in the external circuit (c). The power (d) and voltage (e) could achieve to 453 kW, 17.16 kV, based on a small power source with a volume of 0.256 cm^3 , and the current (f) is 26.4 A, under a shock pressure of 4.93 GPa. The plot (g) of specific power against specific energy for various electrical energy storage devices shows that the force-electric power source based on NBT has a higher power density than other power sources. Compared to PZT and BaTiO_3 ferroelectrics, the power density and energy density of NBT power source are both improved. The data error is $\pm 10\%$.

sample-to-detector distance as well as the orientation of the detector. The x-ray diffraction patterns were collected for 30 s at each pressure, and later integrated over the powder rings to give the conventional one-dimension profile using the FIT2D program [34]. The Le Bail method was used to refine the unit-cell parameters using the GSAS software packages [35]. The lattice parameters of the structure as a function of pressure are shown in Table S2.

D. First-principles simulation

Ab initio calculations are carried out with the Vienna *Ab initio* Simulation Program package (VASP) [36–39] based on density-functional theory with the generalized gradient approximation proposed by Perdew, Burke, and Ernzerhof [40]. The projector augmented-wave method [41] with a cutoff energy of 800 eV is used in the calculations. The Monkhorst-Pack scheme [42] is used to sample the Brillouin zone and the conjugate gradient minimization is used for optimization of the lattice constants and the atom coordinates. We used supercells of 20 atoms with the formula $\text{Na}_2\text{Bi}_2\text{Ti}_4\text{O}_{12}$ for the orthorhombic structure (space group $Pnma$), and 30 atoms with the formula $\text{Na}_3\text{Bi}_3\text{Ti}_6\text{O}_{18}$ for the rhombohedral structure (space group $R3c$). The structures are fully relaxed at each given volume with the k spaces of $8 \times 8 \times 6$ for the orthorhombic and $6 \times 8 \times 4$ for the rhombohedral,

and the convergence of the forces on each atom was less than $0.001 \text{ eV}/\text{\AA}$. Then the meshes of k space were increased to $16 \times 16 \times 12$ and $12 \times 16 \times 8$ to obtain accurate energies by the tetrahedron method with Blöchl corrections [43] after relaxations. The tolerance for the energy convergence was $1 \times 10^{-4} \text{ eV}$.

III. RESULTS AND DISCUSSION

Under different compression pressures, the ferroelectric materials would show different electric output, as shown in Figs. 2(a)–2(c). Here, a shock wave propagated through the sample perpendicular to the P_r direction. In general, the poled ferroelectric ceramics can release all bound charge if the shock pressure is high enough for full depolarization [Fig. 2(a)]. Under these circumstances, the polarization falls to zero following the shock front and a squarelike current wave is observed in the external circuit during shock compression, shown as the red curve in Fig. 2(c) (force-electric effect). The width (w) and amplitude (h) of the current square-wave pulse follow:

$$w = l/v, \quad (4)$$

$$h = \frac{p_r \times l \times n}{l/v} = p_r \times v \times n, \quad (5)$$

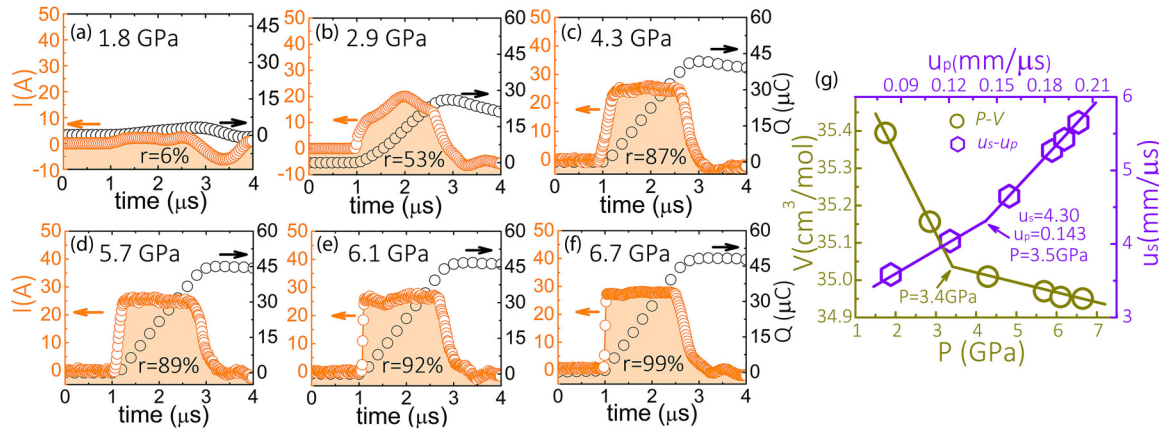


FIG. 3. Current and released charge of NBT ceramics under different shock pressures (a)–(f); with the particle speed–shock wave speed curve (u_s-u_p) and pressure–volume curve ($P-V$) (g). The released charge is calculated from the current data. The r value is the ratio of released charge over the bound charge calculated from P_r .

where v is the speed of the shock wave in the sample, and l , m , and n are the length, thickness, and width of the sample, respectively. Alternatively, if the compression pressure is too low to induce ferroelectric depolarization, P is reduced but with $P \neq 0$ behind the shock-wave front [Fig. 2(b)], and a small and vibrational current is obtained in the external circuit, which is mainly generated by the piezoelectric effect [3,9–11,44], shown as the blue curve in Fig. 2(c). The magnitude of the amplitude of this vibrational current is determined by the piezoelectric constant and the pressure.

In the high power output experiment, a squarelike current wave was observed with a maximum current of 26.4 A, demonstrating that the NBT ferroelectric ceramic depolarized at this pressure. The voltage across the resistor and equivalent power corresponded to 17.16 kV and 453 kW, respectively [Figs. 2(d)–2(f)]. Benefiting from its high P_r , high E_b , and relatively low density, a high power density of 3.04×10^8 W/kg was achieved on NBT ceramic. This power density is higher than most reported force-electric power sources [12,14–19,44–47], and comparable to the peak value on the PZT 95/5 ceramics [9] and $\text{Pb}(\text{In}_{1/2}\text{Nb}_{1/2})\text{O}_3$ – $\text{Pb}(\text{Mg}_{1/3}\text{Nb}_{2/3})\text{O}_3$ – PbTiO_3 single crystal [18]. Considering the NBT sample was not broken down in this study, the power output might further increase with a bigger resistance connected. Figure 2(g) shows the commercially available energy-storage devices to compare with the force-electric effect. The data for the other energy-storage devices are reproduced from the literature [6–8]. The energy density achieved on NBT ceramic is comparable to that of electrical capacitors or supercapacitors, and higher than most of the force-electric power sources [1,2,5,14–19,44–47]. It is worthy to mention that generally we do not compare the ferroelectric generator to other electrical devices, because the force-electric effect could only be used one time, and after shock compression the samples would be mechanically destroyed into pieces, while other devices, such as batteries, are reusable. But, this comparison in Fig. 2(g) can better describe the high power output achieved in this force-electric effect, and this might extend the application of the force-electric effect in the future.

Systematic dynamic experiments were conducted to investigate the energy output behaviors over a range of conditions. Figures 3(a)–3(f) show the current (orange) and total released charge (black) generated from a single piece of ceramic, under varying maximum shock pressures of 1.8, 2.9, 4.3, 5.7, 6.1, and 6.7 GPa, respectively. The amplitude of the current and the total released charge increase with increasing shock pressure. At ~ 1.8 GPa, a typical small piezoelectric effect current is observed. The wave form is vibrational and the highest current reaches no more than 4 A at this pressure. When the pressure is increased to 2.9 GPa, the current can reach about 20 A, while current wave form remains vibrational during the experiment, but appears to be a combination of both the force-electric effect and the piezoelectric effect together. Under these conditions, the pressure is insufficient to fully depolarize the ceramic, and only a fraction of the bound charge is released. A square current wave is observed for shock pressures greater than 4.3 GPa, indicating that depolarization is complete. The parameter r expresses the ratio of actual released charge over the bound charge calculated from P_r [Figs. 3(a)–3(f)]. From these results, the complete depolarization of NBT ceramics could happen above a pressure between 2.9 and 4.3 GPa. The particle speed–shock wave speed curve (u_s-u_p) and pressure–volume relations ($P-V$) are presented in Fig. 3(g). Both the $P-V$ and u_s-u_p curves are discontinuous, indicating a shock-induced phase transition [31,48]. A discontinuity is seen at 3.4 GPa in the $P-V$ curve. On the u_s-u_p curve, a discontinuity is at $u_s = 4.3$ $\text{mm}/\mu\text{s}$, which corresponds to a pressure of $P = 3.5$ GPa. The results suggest that a phase transition happens at 3.4–3.5 GPa, inducing the depolarization of NBT ferroelectric ceramics.

The pressure-dependent structure change of NBT has been studied by x-ray diffraction as a function of pressure, from 0.4 to 9.1 GPa [Fig. 4(a)]. Diffraction peaks, highlighted by a red spade, are observed at 1.5 GPa, indicating the onset of a phase transition. Figure 4(b) shows the normalized $P-V$ curve of NBT (based on a unit cell with $Z = 6$), derived from unit-cell refinements of the XRD data. The results show that NBT is polar phase and rhombohedral (space group $R3c$) at low pressure, and transforms via a first-order phase

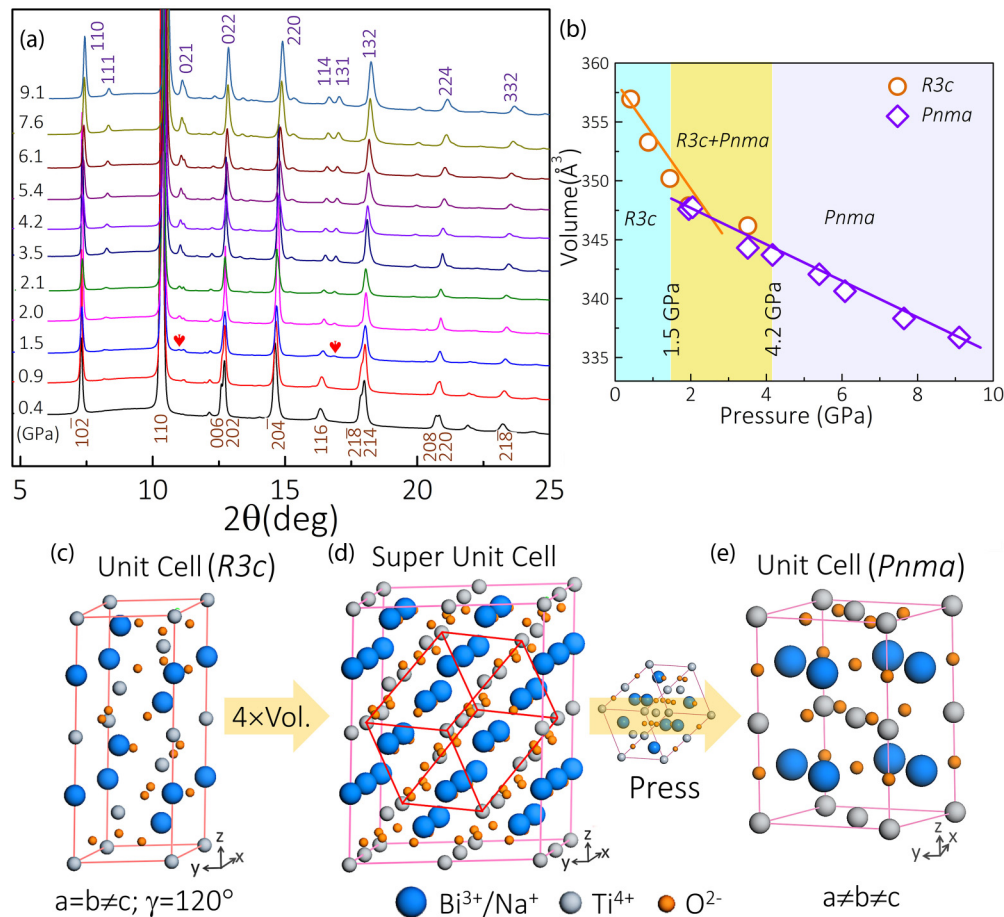


FIG. 4. Pressure dependence of the phase transition in NBT has been studied by the *in situ* synchrotron x-ray diffraction. The x-ray diffraction spectra of NBT ferroelectric materials at selected pressures (a). The XRD peaks of the phase are marked by the red spades. The NBT is rhombohedral (*R3c*) structure at low pressure, and it changes into orthorhombic structure (*Pnma*) at high pressure. The normalized *P-V* curve of NBT according to the $Z = 6$ (b), and the schematic diagram of the structure change during the phase transition is shown in (c)–(e). The red cuboid in (d) is a prototype of the orthorhombic unit cell (*Pnma*) before phase transition in rhombohedral (*R3c*) lattice, which changes into orthorhombic at high pressure (e).

transition to a nonpolar phase (space group *Pnma*), which is orthorhombic and centrosymmetric. The transition commences at 1.5 GPa and phase coexistence persists until the transition is complete at about 4.2 GPa. The electrical output of NBT from depoling under dynamic compression can be attributed to this zone-boundary ferroelectric-to-paraelectric (*R3c*–*Pnma*) phase transition. The relationship between these structures is shown in Figs. 4(c)–4(e). Figure 4(c) shows the unit cell of the *R3c* phase and Fig. 4(d) shows a supercell with doubled *a*- and *b* axes. A prototype of the orthorhombic unit cell (*Pnma*) can be seen in the middle of this supercell, highlighted by a red cuboid, which corresponds to the orthorhombic structure at high pressure shown in Fig. 4(e). Actually, the structures of NBT at high pressure have been investigated in previous studies. The powder-diffraction study at high pressure, by Jones [49], revealed a structural phase transition from rhombohedral (*R3c*) to orthorhombic (*Pnma*) symmetry from ~ 1.0 to ~ 3.3 GPa. The Raman studies at high pressure on NBT by Kreisel *et al.* [50] suggested a transition would happen around 4.5 GPa. Later on, studies on single crystal by Kreisel *et al.* [51] showed that NBT undergoes two phase transitions occurring at different pressures in the

pressure range up to 5 GPa, which are associated with a long-range order change and a short-range order change in the perovskite structures. Our results are in agreement with the previous powder-diffraction and Raman studies considering the experiment error. The difference between powder- and the single-crystal studies might be attributed to the different sample conditions. In general, it is conclusive that the NBT materials undergo a phase transition from a polar rhombohedral structure to an unpolar orthorhombic structure (or monoclinic) below 4.5 GPa.

It should be noted that because pressure-induced depolarization behaviors could be different among ferroelectrics [10,19,52,53], several mechanisms have been developed, such as ferroelectric-antiferroelectric phase transition [10], ferroelectric-paraelectric phase transition [52], ferroelectric domains switch under compression [19], ferroelectric to the ergodic relaxor phase transition [53], etc. However, to clearly figure out the mechanism of shock-induced depolarization is still challenging, because shock compression is fast ($\sim \mu\text{s}$) and the compression zone is an area involving high pressure, high temperature, and high strain rate, but the *in situ* observation method on shock compression area is not available. In this

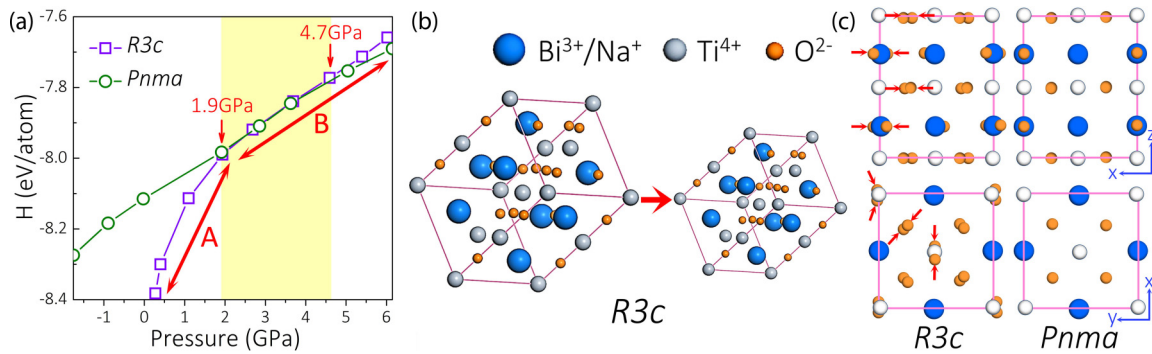


FIG. 5. First-principles calculations of the $R3c$ and $Pnma$ phases as a function of pressure. The enthalpy (H) calculated by first-principles simulation for $R3c$ and $Pnma$ phases at different pressures, respectively (a). The enthalpy change of $R3c$ phase could be divided into two regions (A and B). When the pressure is below 1.9 GPa (region A), the enthalpy of $R3c$ increases sharply due to the volume decreasing, which is shown in (b). When the pressure is above 1.9 GPa (region B), the enthalpy of $R3c$ phase increases gently, which is mainly due to the O^{2-} ions displacing following the red arrows in (c).

study, the ferroelectric-paraelectric phase transition pressure is in a good agreement with the depolarization pressure. Hence, this polar-nonpolar phase transition ($R3c-Pnma$) was believed to be the main contribution for this power output. First-principles calculations have been carried out to determine the enthalpy (H) of the $R3c$ and $Pnma$ phases as a function of pressure [Fig. 5(a)]. The $R3c$ unit cell is depicted as the red cuboid in Fig. 4(d), corresponding to the prototype of the orthorhombic cell ($Pnma$) before the phase transition. The enthalpy of both phases increases with increasing pressure and that of the rhombohedral phase is lower than that of the orthorhombic phase at pressures less than 1.9 GPa. The enthalpies of both phases are similar from 1.9 to 4.7 GPa, where the difference between the enthalpies of two polymorphs is less than 0.1 eV. Above 4.7 GPa, the energy of the $Pnma$ phase is lower, confirming its high-pressure stability. These calculations, alongside our x-ray diffraction results, demonstrate that rhombohedral NBT transforms to orthorhombic at high pressure via a first-order phase transition. Furthermore, the enthalpy change of the $R3c$ phase can be considered over two regions (A and B), below and above 1.9 GPa [Fig. 5(a)]. In region A, the enthalpy increases rapidly, due to rapid volume compression with increasing pressure [Fig. 5(b)]. In region B, the enthalpy increase is gentler, and is mainly the result of small displacements of the polarizable O^{2-} ions within the structure, indicated in Fig. 5(c) by the red arrows. The sublattice of cations in the two structures is similar above 1.9 GPa, and the main difference between the two polymorphs is that the O^{2-} ions in the $R3c$ structure are arranged in zigzag

chains parallel to 001 of the $Pnma$ structure, while these chains become straight in the $Pnma$ structure at high pressure [Fig. 5(c)].

IV. CONCLUSIONS

In conclusion, ferroelectric materials have successfully been applied in energy conversion applications [54–60]. As one fundamental property of the ferroelectrics, the force-electric effect has received attention for years, but materials force-electric studies are sparse and restricted to $BaTiO_3$ and PZT compounds. Here, we have found that the force-electric effect in NBT is larger than that reported for other similar ferroic materials with energy density comparable to that of electrical capacitors or supercapacitors. This high energy output is mainly attributed to a first-order $R-O$ phase transition under high pressure. This phase transition undergoes two steps which correspond to the unit-cell shrink and O^{2-} ions chain rearrangement. These results extend the potential application of the force-electric effects and guide further application and development of ferroelectric materials.

ACKNOWLEDGMENTS

This work was supported by the LSD fund (Grant No. 6142A03010102), LSD engineering project (Grant No. 2016Z-04), CAEP Foundation (Grant No. YZJLX2016001), CSS project (Grant No. YK2015-0602006), and National Natural Science Foundation of China (Grants No. 11704353, No. 11774366, and No. 61475176).

- [1] F. W. Neilson, Effects of strong shocks in ferroelectric materials, *Bull. Am. Phys. Soc.* **2**, 302 (1957).
- [2] R. K. Linde, Depolarization of ferroelectrics at high strain rates, *J. Appl. Phys.* **38**, 4839 (1967).
- [3] S. Shkuratov, J. Baird, and F. Talantsev, The depolarization of $Pb(Zr_{0.52}Ti_{0.48})O_3$ ferroelectrics by cylindrical radially expanding shock waves and its utilization for miniature pulsed power, *Rev. Sci. Instrum.* **82**, 054701 (2011).
- [4] V. N. Zubarev, Impact compression of piezoceramics, *J. Appl. Mech. Tech. Phys.* **12**, 263 (1971).
- [5] B. F. Charles and J. Nation, Ferroelectric sources and their application to pulsed power: A review, *IEEE Trans. Plasma Sci.* **25**, 212 (1997).
- [6] N. Jha, P. Ramesh, E. Bekyarova, M. Itkis, and R. Haddon, High energy density supercapacitor based on a hybrid carbon nanotube-reduced graphite oxide architecture, *Adv. Energy Mater.* **2**, 438 (2012).

- [7] H. Abruna, Y. Kiya, and J. Henderson, Batteries and electrochemical capacitors, *Phys. Today* **61**(12), 43 (2008).
- [8] P. Simon and Y. Gogotsi, Materials for electrochemical capacitors, *Nat. Mater.* **7**, 845 (2008).
- [9] D. Berlincourt, H. Jaffe, and H. Krueger, Release of electric energy in $\text{PbNb}(\text{Zr}, \text{Ti}, \text{Sn})\text{O}_3$ by temperature- and by pressure-enforced phase transitions, *Appl. Phys. Lett.* **3**, 90 (1963).
- [10] M. Avdeev, J. D. Jorgensen, S. Short, G. A. Samara, E. L. Venturini, P. Yang, and B. Morosin, Pressure-induced ferroelectric to antiferroelectric phase transition in $\text{Pb}_{0.99}(\text{Zr}_{0.95}\text{Ti}_{0.05})_{0.98}\text{Nb}_{0.02}\text{O}_3$, *Phys. Rev. B* **73**, 064105 (2006).
- [11] L. L. Altgilbers, J. Baird, B. L. Freeman, C. S. Lynch, and S. I. Shkuratov, *Explosive Pulsed Power* (Imperial College Press, London, 2010).
- [12] Y. Jiang, X. Wang, F. Zhang, and H. He, Breakdown and critical field evaluation for porous PZT 95/5 ferroelectric ceramics under shock wave compression, *Smart Mater. Struct.* **23**, 085020 (2014).
- [13] S. I. Shkuratov, J. Baird, and E. F. Talantsev, Extension of thickness-dependent dielectric breakdown law on adiabatically compressed ferroelectric materials, *Appl. Phys. Lett.* **102**, 052906 (2013).
- [14] S. I. Shkuratov, E. F. Talantsev, and J. Baird, Electric breakdown of longitudinally shocked $\text{Pb}(\text{Zr}_{0.52}\text{Ti}_{0.48})\text{O}_3$ ceramics, *J. Appl. Phys.* **110**, 024113 (2011).
- [15] P. C. Lysne, Shock induced polarization of a ferroelectric ceramic, *J. Appl. Phys.* **48**, 1024 (1977).
- [16] R. Setchell, S. Montgomery, and C. Chhabildas, The effects of shock stress and field strength on shock-induced depoling of normally poled PZT 95/5, *AIP Conf. Proc.* **505**, 979 (2000).
- [17] P. C. Lysne, Resistivity of shock wave compressed PZT 95/5, *J. Appl. Phys.* **48**, 4565 (1977).
- [18] S. I. Shkuratov, J. Baird, V. Antipov, E. Talantsev, J. Chase, W. Hackenberger, J. Luo, H. R. Jo, and C. Lynch, Ultra-high energy density harvested from domain-engineered relaxor ferroelectric single crystals under high strain rate loading, *Sci. Rep.* **7**, 46758 (2017).
- [19] S. I. Shkuratov, J. Baird, V. G. Antipov, W. Hackenberger, J. Luo, S. J. Zhang, C. S. Lynch, J. B. Chase, H. R. Jo, and C. C. Roberts, Complete stress-induced depolarization of relaxor ferroelectric crystals without transition through a non-polar phase, *Appl. Phys. Lett.* **112**, 122903 (2018).
- [20] S. I. Shkuratov, E. F. Talantsev, L. Menon, H. Temkin, J. Baird, and L. L. Altgilbers, Compact high-voltage generator of primary power based on shock wave depolarization of lead zirconate titanate piezoelectric ceramics, *Rev. Sci. Instrum.* **75**, 2766 (2004).
- [21] S. I. Shkuratov, E. F. Talantsev, J. Baird, H. Temkin, L. L. Altgilbers, and A. H. Stults, Longitudinal shock wave depolarization of $\text{Pb}(\text{Zr}_{52}\text{Ti}_{48})\text{O}_3$ polycrystalline ferroelectrics and their utilization in explosive pulsed power, *Shock Compress. Condens. Matter*, **845**, 1169 (2005).
- [22] X. Liu and X. Tan, Giant strains in non-textured $(\text{Bi}_{1/2}\text{Na}_{1/2})\text{TiO}_3$ -based lead-free ceramics, *Adv. Mater.* **28**, 574 (2016).
- [23] M. Li, M. Pietrowski, R. De Souza, H. Zhang, I. Reaney, S. Cook, J. Kilner, and D. Sinclair, A family of oxide ion conductors based on the ferroelectric perovskite $\text{Na}_{0.5}\text{Bi}_{0.5}\text{TiO}_3$, *Nat. Mater.* **13**, 31 (2013).
- [24] See Supplemental Material at <http://link.aps.org/supplemental/10.1103/PhysRevMaterials.3.035401> for experiments supporting information.
- [25] E. Aksel, J. S. Forrester, H. M. Foronda, R. Dittmer, D. Damjanovic, and J. L. Jones, Structure and properties of La-modified $\text{Na}_{0.5}\text{Bi}_{0.5}\text{TiO}_3$ at ambient and elevated temperatures, *J. Appl. Phys.* **112**, 054111 (2012).
- [26] V. A. Isupov, Ferroelectric $\text{Na}_{0.5}\text{Bi}_{0.5}\text{TiO}_3$ and $\text{K}_{0.5}\text{Bi}_{0.5}\text{TiO}_3$ perovskites and their solid solutions, *Ferroelectrics* **315**, 123 (2005).
- [27] D. Maurya, M. Murayama, and S. Priya, Synthesis and characterization of $\text{Na}_2\text{Ti}_6\text{O}_{13}$ whiskers and their transformation to $(1-x)\text{Na}_{0.5}\text{Bi}_{0.5}\text{TiO}_3-x\text{BaTiO}_3$ ceramics, *J. Am. Ceram. Soc.* **94**, 2857 (2011).
- [28] M. Li, L. Li, J. Zang, and D. C. Sinclair, Donor-doping and reduced leakage current in Nb-doped $\text{Na}_{0.5}\text{Bi}_{0.5}\text{TiO}_3$, *Appl. Phys. Lett.* **106**, 102904 (2015).
- [29] D. D. Koller, R. S. Hixson, G. T. Gray III, P. A. Rigg, L. B. Addessio, E. K. Cerreta, J. D. Maestas, and C. A. Yablinsky, Influence of shock-wave profile shape on dynamically induced damage in high-purity copper, *J. Appl. Phys.* **98**, 103518 (2005).
- [30] S. S. Mokrushin, E. I. Karnaukhov, S. N. Malugina, D. N. Kazakov, O. E. Kozelkov, and A. V. Pavlenko, Research of dynamic properties of alloys of AMg_6BM and AMg_6M in shock-wave experiment on a gas gun, *EPJ Web Conf.* **94**, 01055 (2015).
- [31] R. Cheret, P. Andriot, P. Chapron, C. Le Drean, J. M. Lezaud, R. Loichot, J. Martineau, and F. Olive, Shock-wave experiments using explosives and light-gas gun facilities, *AIP Conf. Proc.* **78**, 626 (1982).
- [32] H. Tan, *Introduction to Experimental Shock-wave Physics* (National Defense Industry Press, Beijing, China, 2007).
- [33] V. Zharkov and V. Kalinin, *Equation of State for Solids at High Pressures and Temperature* (Consultants Bureau, New York, 1971).
- [34] J. Hammersley, FIT2D Report (Europe Synchrotron Radiation Facility, Grenoble, France, 1996).
- [35] L. B. McCusker, R. B. Von Dreele, D. E. Cox, D. Louër, and P. Scardi, Rietveld refinement guidelines, *J. Appl. Cryst.* **32**, 36 (1999).
- [36] G. Kresse and J. Hafner, *Ab initio* molecular dynamics for liquid metals, *Phys. Rev. B* **47**, 558 (1993).
- [37] G. Kresse and J. Hafner, *Ab initio* molecular-dynamics simulation of the liquid-metal-amorphous-semiconductor transition in germanium, *Phys. Rev. B* **49**, 14251 (1994).
- [38] G. Kresse and J. Furthmüller, Efficiency of *ab-initio* total energy calculations for metals and semiconductors using a plane-wave basis set, *Comput. Mater. Sci.* **6**, 15 (1996).
- [39] G. Kresse and J. Furthmüller, Efficient iterative schemes for *ab initio* total-energy calculations using a plane-wave basis set, *Phys. Rev. B* **54**, 11169 (1996).
- [40] J. Perdew, K. Burke, and M. Ernzerhof, Generalized Gradient Approximation Made Simple, *Phys. Rev. Lett.* **77**, 3865 (1996).
- [41] G. Kresse and D. Joubert, From ultrasoft pseudopotentials to the projector augmented-wave method, *Phys. Rev. B* **59**, 1758 (1999).
- [42] H. Monkhorst and J. Pack, Special points for Brillouin-zone integrations, *Phys. Rev. B* **13**, 5188 (1976).

- [43] P. Blöchl, O. Jepsen, and O. Andersen, Improved tetrahedron method for Brillouin-zone integrations, *Phys. Rev. B* **49**, 16223 (1994).
- [44] C. Reynolds and G. Seay, Two wave shock structures in the ferroelectric ceramics barium titanate and lead zirconate titanate, *J. Appl. Phys.* **33**, 2234 (1962).
- [45] I. Fritz, Ultrasonic, dilatometric, and dielectric study of uniaxial stress effects in a barium calcium titanate ceramic, *J. Appl. Phys.* **49**, 788 (1978).
- [46] D. Doran, Shock-wave compression of barium titanate and 95/5 lead zirconate titanate, *J. Appl. Phys.* **39**, 40 (1968).
- [47] P. C. Lysne and C. Percival, Electric energy generation by shock compression of ferroelectric ceramics: Normal mode response of PZT 95/5, *J. Appl. Phys.* **46**, 1519 (1975).
- [48] W. J. Carter, Relation between dynamic and static phase transformation studies, in *Metallurgical Effects at High Strain Rates*, edited by R. W. Rohde, B. M. Butcher, J. R. Holland, and C. H. Karnes (Springer, Boston, MA, 1973), p. 171.
- [49] G. O. Jones, Ph.D. thesis, University of Warwick, 2001.
- [50] J. Kreisel, A. Glazer, P. Bouvier, and G. Lucazeau, High-pressure Raman study of a relaxor ferroelectric: The $\text{Na}_{0.5}\text{Bi}_{0.5}\text{TiO}_3$ perovskite, *Phys. Rev. B* **63**, 174106 (2001).
- [51] J. Kreisel, P. Bouvier, B. Dkhil, P. A. Thomas, A. M. Glazer, T. R. Welberry, B. Chaabane, and M. Mezouar, High-pressure x-ray scattering of oxides with a nanoscale local structure: Application to $\text{Na}_{1/2}\text{Bi}_{1/2}\text{TiO}_3$. *Phys. Rev. B* **68**, 014113 (2003).
- [52] K. H. Cho, E. S. Chang, Y. S. Choi, Y. H. Ko, and K. J. Kim, Effect of pressure on electric generation of PZT(30/70) and PZT(52/48) ceramics near phase transition pressure, *J. Eur. Ceram. Soc.* **32**, 457 (2012).
- [53] P. Peng, H. Nie, G. Wang, Z. Liu, F. Cao, and X. Dong, Shock-driven depolarization behavior in BNT-based lead-free ceramics, *Appl. Phys. Lett.* **113**, 082901 (2018).
- [54] B. Naranjo, J. Gimzewski, and S. Putterman, Observation of nuclear fusion driven by a pyroelectric crystal, *Nature (London)* **434**, 1115 (2005).
- [55] L. Martin and A. M. Rappe, Thin-film ferroelectric materials and their applications, *Nat. Rev.* **2**, 16087 (2017).
- [56] B. Neese, B. Chu, S. Lu, Y. Wang, E. Furman, and Q. Zhang, Large electrocaloric effect in ferroelectric polymers near room temperature, *Science* **321**, 821 (2008).
- [57] X. Moya, S. Kar-Narayan, and N. Mathur, Caloric materials near ferroic phase transitions, *Nat. Mater.* **13**, 439 (2014).
- [58] W. Yang, J. Noh, N. Jeon, Y. Kim, S. Ryu, J. Seo, and S. Seok, High-performance photovoltaic perovskite layers fabricated through intramolecular exchange, *Science* **348**, 1234 (2015).
- [59] D. Grupp and A. Goldman, Giant piezoelectric effect in strontium titanate at cryogenic temperatures, *Science* **276**, 392 (1997).
- [60] Z. Xiong and L. Cao, Interparticle spacing dependence of magnetic anisotropy and dipolar interaction of Ni nanocrystals embedded in epitaxial BaTiO_3 matrix, *Ceram. Int.* **44**, 8155 (2018).